GPGPU-BASED 3-D HYBRID FEM/DEM FOR NUMERICAL MODELLING OF VARIOUS ROCK TESTING METHODS

D. Fukuda[a, b], M. Mohammadnejad[a], H. Liu[a*], S. Cho[c], S. Oh[c], G. Min[c], A. Chan[a], J. Kodama[b], F. Fujii[b]

[a] School of Engineering AMC, University of Tasmania, Hobart, Australia
[b] Hokkaido University, Sapporo, Japan
[c] Chonbuk National University, Jeonju, Korea
[*] Corresponding author

ABSTRACT

In the field of geotechnical engineering, the number of applications of combined/hybrid finite-discrete-element method (HFDEM) to both the lab-scale and field-scale problems has increased recently. In author's research group at university of Tasmania, 2-D/3-D HFDEM code has also been successfully developed [e.g. Liu et al. 2015, Int. J. Geotech. Eng. 9:115-131] and applied to some geotechnical engineering problems such as rock blasting, fracture processes in a series of lab-scale rock testing methods and asperity degradation and gouge grinding during direct shearing of rough rock joints. However, since the HFDEM code was implemented by sequential programming, its main application mentioned above was limited to 2-D problems owing to the computationally expensive nature of HFDEM. To overcome this situation, the parallel programming scheme using "general-purpose-graphic-processing-unit (GPGPU)" and "CUDA (Compute Unified Device Architecture) C" was recently incorporated into the HFDEM code and significant speed-up has been achieved. This paper briefly describes the theory and newly incorporated features of the GPGPU-based HFDEM code along with some important issues which have not been addressed clearly in the previous publications using HFDEM. Then, this paper demonstrates some examples of 3-D numerical modelling of rock fracture process using various lab-scale rock testing methods such as quasi-static Brazilian test, quasi-static uniaxial compression test, dynamic Brazilian test using Split Hopkinson Pressure Bar (SHPB) apparatus. Through these demonstrations, the applicability of the newly developed 3-D HFDEM code is shown.

1 INTRODUCTION

Understanding the mechanism of the fracture process in rocks is important in the field of geotechnical engineering. Application of numerical methods has dramatically increased recently for investigation of the fracture process of rocks and the mechanism of rock fracture. For a realistic simulation of the fracture process of rock, numerical techniques should be capable of capturing crack onset and arbitrary crack growth, correct crack length within a given time interval as well as the propagating directions. In recent years, increasing attention has been paid on the techniques which combines/couples the advantages of the continuum-based and discontinuum-based numerical methods. The combined finite-discrete element method (FEM/DEM) proposed by Munjiza (2004) has been employed successfully to model problems dealing with transition process from continuum to discontinuum such as rock fracturing and fragmentation (Mohammadnejad et al, 2018). Y(2D/3D) code (Munjiza, 2004) and ELFEN(2D/3D) (Rockfield, 2005) are two main implementations of the combined FEM/DEM. Several attempts have been made to extend the Y code such as Y-GEO (Mahabadi et al, 2012), IRAZU(Lisjak et al, 2018), SOLIDITY (Xiang et al, 2016) , HOSS with MUNROU (Rougier et al, 2014) and authors' 2D/3D Y-HFDEM IDE (integrated development environment) (Liu et al, 2015). The principles of the combined FEM/DEM are based on continuum mechanics, cohesive zone modelling and contact mechanics which make it computationally expensive. In fact, many of the previous research works applying the combined FEM/DEM have focused on 2D problems rather than 3D problems owing to the expensive computational cost for the combined FEM/DEM. Therefore, developing a capable parallel computation schemes is indispensable in order to deal with larger scale problems with massive number of nodes, elements and contact interactions.

To date some successful parallel implantations of the combined FEM/DEM codes using MPI (message-passing-interface) and shared memory programming with OpenMP have been reported (Lukas et al, 2014; Rougier et al, 2014; Xiang et al, 2016). The MPI needs a large and expensive PC cluster to achieve the best performance. Meanwhile, the OpenMP assumes shared memory in a PC or workstation and thus its application is limited to the total number of multi processors and memory size in the computer, and the MPI is still required for large scale problems in which each PC or workstation uses the OpenMP. Additionally, the application of GPGPU (General Purpose Graphic Processing Unit) controlled by

either OpenCL or CUDA (Compute Unified Device Architecture) can be considered as another promising method since the thousands of core processors can reside and concurrently work in a small GPGPU board within an ordinary PC or workstation. The concept of GPGPU cluster with massive number of GPGPU boards is also possible. The GPGPU-based commercial code IRAZU (Lisjak et al, 2018) recently developed/applied GPGPU with OpenCL to parallelize the combined FEM/DEM and successfully showed a good potential of GPGPU for the combined FEM/DEM simulations for 2D/3D problems. However, the applicability of GPGPU-based combined FEM/DEM using CUDA has not been investigated enough yet.

This paper aims to explain the algorithm of recently developed 3D Y-HFDEM IDE parallelized by GPGPU with CUDA C/C++ in rather detail, along with some demonstrations of 3D numerical modelling of fracture process in various rock testing methods using the developed GPGPU-based code.

2 3D Y-HFDEM IDE

The Y-HFDEM 2D/3D IDE was originally developed using object-oriented programming in visual C++ (Liu et al, 2015) on the basis of the CPU-based sequential open-source Y-code (Munjiza, 2004). The Y-HFDEM 2D/3D IDE not only can significantly simply the process of building and manipulating the input models and greatly reduce the possibility of erroneous model setup, but also can display the calculated results graphically in real-time with OpenGL. The pre-processor of the Y-HFDEM IDE can even generate simple FEM/DEM mesh and specify the initial conditions, physical properties, contact properties, boundary conditions, fracture criteria, and explosive charges if necessary. More complex FEM/DEM meshes are usually generated using third party software. Then, the generated mesh data can be easily imported into the Y-HFDEM IDE for the combined FEM/DEM analyses. The post-processor can visually display the calculated stress, displacement, velocity, force, damage, fracture and fragmentation in real-time pictures or query calculated results in specified locations and graphically display them. In addition, a number of operations such as pan, rotation, zoom, various viewports in perspective and/or orthographic modes, and slideshow are developed to manipulate the numerical models and calculated results (see Liu et al, 2015 for further detail). Because of the nature of the sequential programming, its main application was limited to small scale 2D problems using relatively rough mesh. To overcome this limitation, the parallel programming scheme using the GPGPU controlled by CUDA C/C++ is implemented into the code through this study. Since the various combined FEM/DEM-based codes have been independently developed in each research institute/organization and have different features, the fundamental features of Y-HFDEM 3D IDE along with its GPGPU-based parallelization scheme are explained in detail through the following subsections.

2.1 FUNDAMENTAL THEORY OF 3D Y-HFDEM IDE

The principles of the combined FEM/DEM are based on continuum mechanics, cohesive zone modelling and contact mechanics, all of which are formulated in the framework of explicit FEM.

The continuum behavior of materials including rocks is modeled by an assembly of continuum 4−node tetrahedral finite elements (TET4s) (Fig. 1(a)). Either isotropic or anisotropic elastic solid with viscous damping can be considered. Currently, 3D Y-HFDEM IDE has two options for elastic constitutive equations. In the option 1, the elastic solid obeys Eq. (1) of Neo-Hookean elastic model, which has been widely used in open-source Y-code.

$$\sigma_{ij} = \frac{\lambda}{2}\left(J - \frac{1}{J} \right)\delta_{ij} + \frac{\mu}{J}\left(B_{ij} - \delta_{ij} \right) + \eta D_{ij} \quad (i, j = 1, 2, 3) \tag{1}$$

where σ_{ij} denotes the Cauchy stress tensor, B_{ij} is the left Cauchy-Green strain, λ and μ are the Lame's constants, J is the determinant of deformation gradient, η is the damping coefficient and D_{ij} is the rate of deformation tensor. In this option, only isotropic elastic behavior is considered. On the other hand, in the option 2, the elastic solid obeys Eq. (2) of hyper elastic model.

$$S_{KL} = C_{KLMN} E_{MN} \, (K, L, M, N = 1, 2, 3), \quad \sigma_{ij} = \frac{1}{J} F_{iK} S_{KL} F_{jL} + \eta D_{ij} \quad (i, j, K, L = 1, 2, 3) \tag{2}$$

where S_{KL} denotes the 2nd Piola-Kirchhoff stress tensor, C_{KLMN} is the effective elastic stiffness tensor, E_{MN} is the Green-Lagrange strain tensor, F_{iK} is the deformation gradient. Note that the Einstein's summation convention applies in Eqs. (2). By setting C_{KLMN} in Eq. (2) properly, isotropic and anisotropic elastic behaviors can be considered. In both of these two options, large displacement and large rotation can be simulated. The 3D Y-HFDEM IDE can deal with both dynamic and quasi-static problems. For the simulation of fracture process of materials under quasi-static loading, $\eta = \eta_{\text{crit}} = 2h\sqrt{(\rho E)}$ is used to approximately achieve critical damping, where h, ρ and E are the element length, density and Young's modulus of the target material, respectively. The σ_{ij} within each TET4 is converted to the equivalent nodal force $\mathbf{f}_{\text{int}}$.

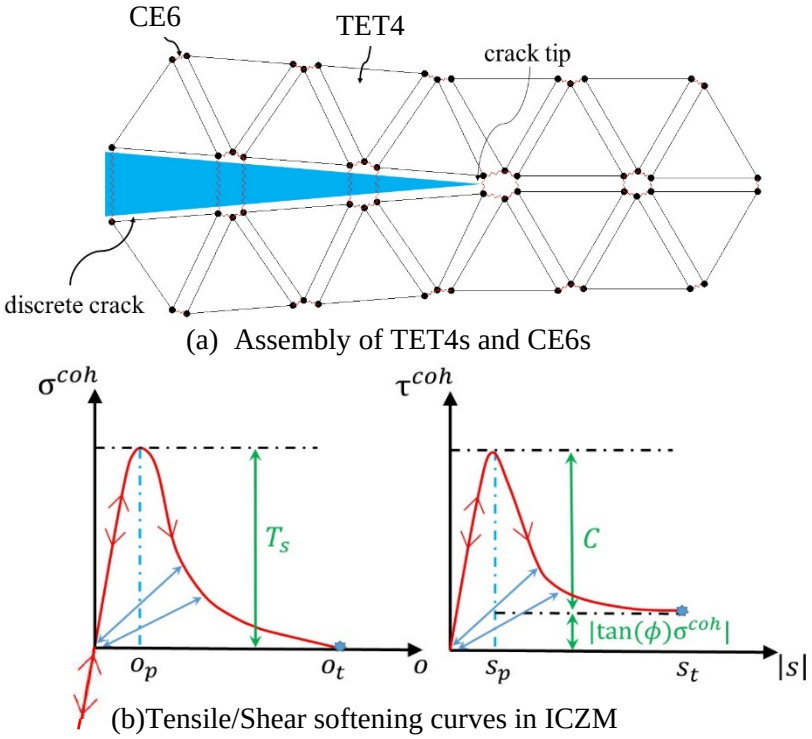

Figure 1: Modelling of transition from continuum to discontinuum behaviour of rock in HFDEM code.

Fracturing of rock under mode I and mode II loading conditions, i.e. opening and sliding of cracks, is modeled through CZM with the concept of smeared crack. To model the behavior of the fracture process zone in front of the crack tips, tensile and shear softening is applied using an assembly of 6−node initially zero−thickness cohesive elements (CE6s) (Fig. 1(a)) as a function of crack opening and sliding displacements, (o, s), respectively (Fig. 1(b)). Two methods can be used for the insertion of the CE6s. One is to insert the CE6s into all the boundary of the TET4s at the beginning of the analysis which is known as intrinsic cohesive zone model (ICZM) and the second is to adaptively insert the CE6s into the particular boundaries of the TET4s with the help of adaptive remeshing techniques where given failure criterion is met, which is referred as extrinsic cohesive zone model (ECZM). Many existing combined FEM/DEM codes, e.g. Y code including 2D/3D Y-HFDEM IDE, have employed the ICZM while some codes such as ELFEN uses the ECZM. One of the advantages of the ICZM is that the implementation and application of parallel computing algorithm is straightforward, meanwhile an "artificial" elastic behavior of CE6s before the onset of fracturing must be specified which requires the introduction and correct estimation of penalty terms and careful selection of time-step increment, Δt, to avoid numerical instability. Although we have already developed GPGPU-based 3D Y-HFDEM IDE using ECZM as well, this paper focuses on only 3D Y-HFDEM IDE using ICZM because of the page limitation and few verifications/validations for the ECZM approach have been conducted yet.

In the GPGPU-based 3D Y-HFDEM code using ICZM, normal and shear cohesive tractions, (σ^{coh} and τ^{coh}, respectively), acting on each face of CE6 are computed using Eq. (3) assuming tensile and shear softening behaviors, respectively:

$$\sigma^{coh}=\begin{cases}\dfrac{2o}{o_{\text{overlap}}}T_s & \text{if } o<0\\ \left[\dfrac{2o}{o_p}-\left(\dfrac{o}{o_p}\right)^2\right]f(D)T_s & \text{if } 0\le o\le o_p\\ f(D)T_s & \text{if } o_p<o\end{cases},\ \tau^{coh}=\begin{cases}-\sigma^{coh}\tan(\phi)+\left[\dfrac{2|s|}{s_p}-\left(\dfrac{|s|}{s_p}\right)^2\right]f(D)c & \text{if } 0\le|s|\le s_p\\ -\sigma^{coh}\tan(\phi)+f(D)c & \text{if } s_p<|s|\end{cases} \tag{3}$$

where o_p and s_p are the elastic limits of o and s, respectively, o_{overlap} is the representative overlapping when o is negative, T_s is the tensile strength of CE6, c is the cohesion of CE6 and ϕ is the internal friction angle of CE6. Positive o and σ^{coh} mean crack opening and tensile cohesive traction, respectively. Modelling τ^{coh} in Eq. (3) corresponds to the Mohr-Coulomb (MC) shear strength model with tension cut-off. The "artificial" elastic behavior of each CE6 characterized by o_p and s_p along with o_{overlap} is necessary, when ICZM is used, to connect the TET4s to express the intact deformation process, which is given as follows (Munjiza et al, 1998):

$$o_p = 2hT_s / P_f \ , s_p = 2hc / P_{\tan} \ , o_{overlap} = 2hT_s / P_{overlap} \tag{4}$$

where P_f, $P_{\tan}$ and $P_{overlap}$ are the penalty terms for opening in normal direction, sliding in tangential direction and overlapping in normal direction, respectively, and h is the element length. The values of the penalty terms can be considered as the stiffness of the CE6 for its opening, sliding and overlapping, respectively. Ideally, their values should be infinity to satisfy elastic behavior of rocks according to Eqs. (1) or (2), while this requires the infinitesimal Δt. Therefore, a reasonably large value of the penalty terms, compared to the Young's modulus or Lame's constants, are required since it is impossible to use infinity in actual numerical simulations. Otherwise, the intact behavior of the bulk rock shows significantly different behavior from that specified by Eqs. (1) or (2) and therefore the elastic constants used in Eqs. (1) or (2) loses their meaning. This is a very important matter, especially for the problems in which the speed of stress wave is an important factor. The function, $f(D)$, in Eq. (3) is the characteristic function for tensile and shear softening curves (Fig. 1(b)) depending on a damage value D of the CE6. The following definitions of D and $f(D)$ are used to consider not only the mode I and II fracturing modes but also a mixed mode I-II fracturing mode:

$$D = \text{Minimum}\left(1, \sqrt{\left(\frac{o-o_p}{o_t}\right)^2 + \left(\frac{|s|-s_p}{s_t}\right)^2}\right) \text{ if } o \ge o_p \text{ or } |s| > s_p \text{ , otherwise 0} \tag{4}$$

$$f(D) = \left[1 - \frac{A+B-1}{A+B}\exp\left(D\frac{A+CB}{(A+B)(1-A-B)}\right)\right]\left[A(1-D) + B(1-D)^C\right] \quad (0 \le D \le 1) \tag{5}$$

where A, B and C are the intrinsic rock properties which determine the shape of softening curves, o_t and s_t are the critical values of o and s, respectively, in which a CE6 breaks and turns to a macro/explicit fracture. To avoid unrealistic damage recovery, i.e. the increase of f, the following new treatment has been implemented into the code. If the trial f computed from Eq. (5) at the current time step becomes larger than that at previous time step, f_{pre}, a condition of $f = f_{pre}$ is assigned to avoid the unrealistic damage recovery. The o_t and s_t in Eq. (4) satisfy the Mode I and II fracture energies G_{fI} and G_{fII} specified in Eqs. (6):

$$G_{fI} = \int_{o_p}^{o_t} \sigma^{coh}(o)\mathrm{d}o \quad , G_{fII} + W_{res} = \int_{s_p}^{s_t} \left\{\tau^{coh}(|s|)\right\} \mathrm{d}|s| \tag{6}$$

where W_{res} is the amount of work per area of CE6 done by the residual stress term in the MC shear strength model. This paper uses the same $f(D)$ with A, B and C equal to 0.63, 1.8 and 6.0, respectively, for both mode I and II fracture processes. In addition, unloading, i.e. the decrease of o or |s|, can also occur during the softening regime, i.e. o>op or |s|>sp (see Fig. 1(b)), which is modeled based on Eqs. (7) and (8):

$$\sigma^{coh} = f(D_{\max})T_s \frac{o}{o_{\max}} \text{ if } 0 < o < o_{\max} \text{ and } o_{\max} > o_p \tag{7}$$

$$\tau^{coh} = \left\{-\sigma^{coh}\tan(\phi) + f(D_{\max})c\right\}\frac{|s|}{s_{\max}} \text{ if } |s| < s_{\max} \text{ and } s_{\max} > s_p \tag{8}$$

In each CE6, the computed σ^{coh} and τ^{coh} are converted to the equivalent nodal force $\mathbf{f}_{coh}$ using 3-point or 7-point Gaussian integration scheme in the current implementation. When either o_t or s_t is achieved in a CE6, the element becomes deactivated and its surfaces can be considered as new macro fracture surfaces.

The contact processes between the material surfaces including the newly created macro fractures by the separation of each CE6 are modeled by the penalty method (Munjiza, 2004) and the complete and excellent explanation of the method is given in the literature. As a brief explanation, when any two TET4 elements subjected to contact detection (see next subsection for the implementation of contact detection in the framework of GPGPU) are found to be overlapped with each other, the contact potential due to the overlapping of the two TET4s, i.e. the contacting couple, is exactly computed. The normal contact force, f_{con_n}, is then computed for each contacting couple, which is normally acting on the contact surface and is proportional to the contact potential. The proportional factor is called normal contact penalty, P_{n_con}. After f_{con_n} is determined, tangential contact force, f_{con_tan}, is computed according to classical quasi-static Coulomb friction law. First, the trial tangential contact force is computed by $(f_{con\_tan})^{trial} = (P_{tan\_con} \times \Delta u_{slide})$ where P_{tan_con} is a tangential contact penalty. The actual f_{con_tan} is computed based on Eq. (9):

$$f_{con\_tan} = \begin{cases} \left(f_{con\_tan}\right)^{trial} & \text{if } \left(f_{con\_tan}\right)^{trial} \le \mu_{fric} f_{con\_n} \\ \mu_{fric} f_{con\_n} & \text{if } \left(f_{con\_tan}\right)^{trial} > \mu_{fric} f_{con\_n} \end{cases} \tag{9}$$

where μ_{fric} is the friction coefficient between the contact surfaces. The tangential contact force, f_{con_tan}, is applied parallel to the contact surface against the direction of the relative sliding of the contact faces. In each contacting couple, the contact force is converted to the equivalent nodal force $\mathbf{f}_{con}$.

By computing the nodal forces mentioned above, the following equation of motion, Eq. (10), is obtained and solved in the framework of explicit FEM:

$$\mathbf{M}\partial^2\mathbf{u} / \partial t^2 = \mathbf{f}_{ext} + \mathbf{f}_{int} + \mathbf{f}_{coh} + \mathbf{f}_{con} \tag{10}$$

where **M** is a lumped nodal mass, u is the nodal displacement and $\mathbf{f}_{ext}$ is the nodal force corresponding to the external load. The central difference scheme is employed for the explicit time integration to solve Eq. (10).

2.2 GPGPU-BASEDBASED PARALLELIZATION OF 3D Y-HFDEM IDE BY CUDA C/C++

To speed−up simulation process of the 3D Y-HFDEM IDE, a parallel computation scheme based on the NVIDIA GPGPU accelerator controlled through the NVIDIA's CUDA C/C++ is incorporated. In CUDA programming, functions also known as "*kernels*" launched on the GPGPU device are executed by multiple "*threads*" in multiple "*Blocks*". Each "*thread*" in each "*block*" is just an execution unit of a "*kernel*" with a unique "*index*". In the GPGPU implementation of 3D Y-HFDEM IDE, computations of each TET4($\mathbf{f}_{int}$), CE6($\mathbf{f}_{coh}$), contact couple($\mathbf{f}_{con}$) and nodal equation of motion (Eq. (10)) are assigned to each CUDA "*thread*" in each "*block*" and processed in a massively parallel manner. For the achievement of the efficient contact detection for identifying each contacting couple, a domain decomposition algorithm is adapted. In this algorithm, analysis domain comprising a massive number of TET4s are subdivided into multiple equal−sized (n_x, n_y, n_z) cubic sub−cells so that the largest TET4 in the model is completely included in a single sub−cell. In this way, every TET4 can have a corresponding single sub−cell to which it belongs. By using integer coordinate (ix, iy, iz) (ix=0,⋯,n_x-1, iy=0,⋯,n_y-1, iz=0,⋯,n_z-1) for the location of each sub−cell and by assigning unique hash values ($iz\times n_y\times n_x+iy\times n_x+ix$) to each integer coordinate of each sub−cell, the data of TET4 element IDs are sorted according to the hash values as key. Thus, for each sub−cell, the TET4 element IDs included in the sub−cell can be readily available in this method. The radix sorting algorithm optimized for CUDA implemented in thrust library is used for the key−sorting by hash. Thus, for a particular cubic cell, only searching its adjacent 27 cells for contact detection is sufficient and this makes it possible to achieve efficient contact detection only on the GPGPU. Therefore, the proposed GPGPU code can run in "completely parallel" on the GPGPU and no sequential processing is necessary, except for the input and output procedures since data transfer from the GPGPU to the host computer is necessary for these. The obtained results can be visualized either in OpenGL implemented in the code (Liu et al, 2015) or any versions of open source visualization software Paraview (Ayachit, 2015). In the following demonstrations in section 3, NVIDIA GPGPU accelerator "Quadro GP100 (Pascal generation)" was used.

3 EXAMPLES OF NUMERICAL MODELLING

3.1 ROCK LABORATORY TESTS

In order to verify the capabilities of the code in simulating rock fracture process and associated failure mechanism, this section models two standard laboratory rock mechanics tests, i.e. Brazilian test and Uniaxial Compression Test (UCS) using the GPGPU-parallelized 3-D hybrid FEM/DEM. To this purpose, the failure processes of a relatively soft rock in these two tests are modelled. The physical-mechanical properties of the rock and the numerical input parameters used in the numerical simulation are listed in Table 1.

Table 1: Rock mechanical properties and numerical parameters

Parameter	*Unit*	*Value*
Density (ρ)	Kg/m3	1800
Young's modulus (E)	GPa	12.2
Poisson's ratio (v)	-	0.25
Tensile strength (T_s)	MPa	1.6
Cohesion (c)	MPa	4.5
Internal Friction angle of intact rock (φ)	°	25
Mode I fracture energy (G_{fI})	J/m^2	2.7
Mode II fracture energy (G_{fII})	J/m^2	27
Normal contact penalty number (P_{n_con})	GPa	1220
Tangent contact penalty number (P_{tan_con})	GPa/m	1220
Fracture penalty numbers ($P_{overlap}$)	GPa/m	12200

In the numerical model of the uniaxial compression test, the height and diameter of the rock specimen are 129.5 mm and 51.7 mm, respectively. The numerical model consists of 695428 unstructured TET4s (Fig. 2(a)). The diameter and thickness of the Brazilian Disc (BD) are 51.7 mm and 25.95 mm, respectively, and the numerical model consists of 171209 unstructured TET4s (Fig.2(b)). The average edge length of TET4s in both models is 1.2 mm. The rock specimens are placed between two moving rigid platens with a constant velocity of 0.05 m/s to satisfy quasi-static loading conditions [17]. The friction coefficient between platens/rock and rock/rock are assumed to be 0.1 and 0.5, respectively [52].

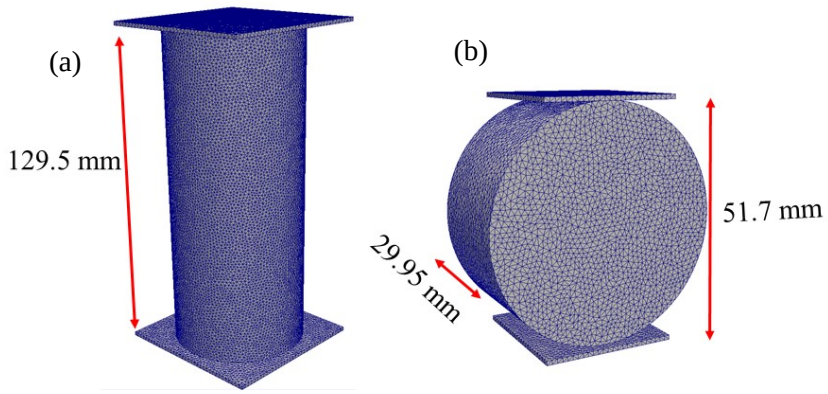

Figure 2: Model geometry and mesh discretization for laboratory tests: a) Brazilian test, b) Uniaxial compression test

Fig. 3(a) illustrates the horizontal stress distribution, σxx, along the diameter of the BD before the macroscopic splitting/tensile failure is initiated. Hereafter, compressive stress is shown as negative (cold colour) while tension stress is regarded as positive (warm colour). When the concentrated stress reaches the critical value (i.e. the tensile strength of the rock), tensile failure develops in the model (Fig. 3(b)). With the two loading plates further moving to each other, the splitting failure of the BD occurs due to the propagation of the formed macroscopic fractures, which coalesce with the microcracks initiated due to the resultant tension stresses during the propagation process. Fig. 3(d) depicts the axial stress versus axial strain curve obtained from the simulation of the Brazilian test using the GPGPU-parallelized hybrid FEM/DEM. Obtained results from GPGPU-parallelized 3-D hybrid FEM/DEM can realistically model the splitting/tensile failure process of rock in the Brazilian test.

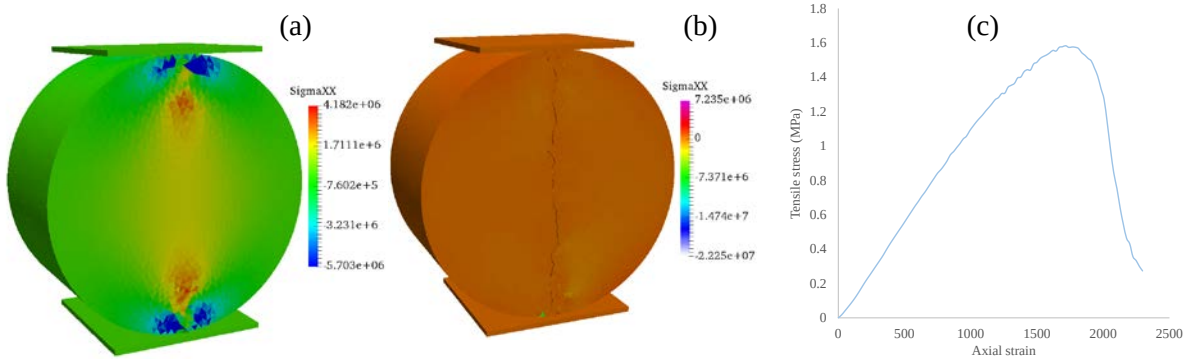

Figure 3: The results of numerical simulation of Brazilian test. (a) Horizontal stress distribution, (b) post failure fracture pattern and corresponding horizontal stress distribution, (d) Brazilian indirect tensile stress versus axial strain.

Fig. 4 (a) illustrates the stress building-up and evolutation process before the onset of nonlinearity in the stress-axial strain curve. As the loading continues, unstable micro crack growth commences and continues to the peak stress point of the stress-strain curve (Fig. 4(c)). After that, the microcracks coalesce with each other to form macroscopic cracks, which results in the rock specimen loses its bearing capacity and correspondingly the observed stress decreases with the strain increasing. Finally, the formed macroscopic cracks further propagate resulting in the rock specimen completely loses its

bearing capacity as shown in Fig. 4(b). It is obvious that the developed GPGPU-parallelized 3-D hybrid FEM/DEM code is able of realistically modelling the shear dominant failure process of rock under the uniaxial compression test.

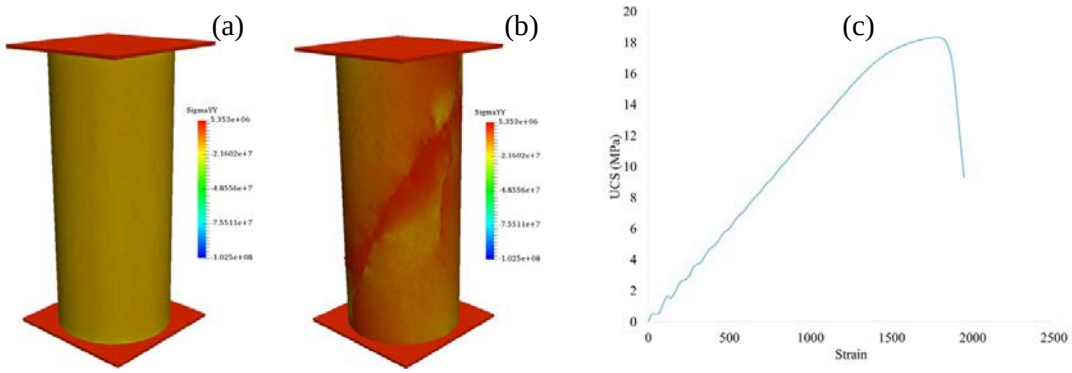

Figure 4: The results of numerical simulation of UCS. (a) Axial stress distribution, (b) post failure fracture pattern and corresponding axial stress distribution, (d) Brazilian indirect tensile stress versus axial strain.

3.2 ROCK TESTING METHODS USING DYNAMIC LOADING

Authors have recently started working on modelling various dynamic rock testing methods such as spalling test using Hopkinson pressure bar (HPB) apparatus (Fig. 5(a)) and dynamic Brazilian test using a split Hopkinson pressure bar (SHPB) apparatus (Fig. 5(b)), among many examples. A common procedure for these two methods is that a metal projectile, i.e. striker bar (SB), is accelerated by a gas gun and strikes one end of a long cylindrical metal bar, i.e. incident bar (IB). Upon the impact, dynamic compressive wave, σ_{inci}, is induced in the IB. The σ_{inci} propagates toward the other end of the IB in which the target rock specimen is placed. When the σ_{inci} arrives at the interface between the IB and rock specimen, some of the σ_{inci} is reflected as tensile stress wave, σ_{refl}, and remaining portion of σ_{inci} is transmitted into the rock specimen as compressive transmitted wave, σ_{tans}. In the case of spalling test using the HPB (Fig. 5(a)), the σ_{tans} propagates toward the free end of the cylindrical rock specimen in the way that the stress level of σ_{tans} does not exceed the compressive strength of the target rock but its amplitude is large enough compared with its tensile strength. When

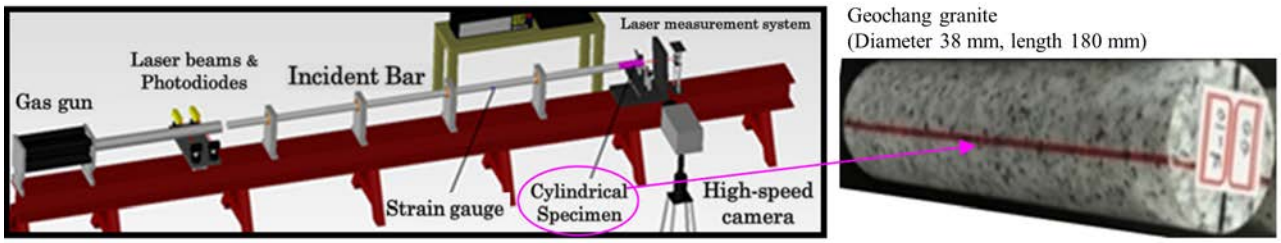

(a) Configuration of HPB-based spalling test for Geochang granite

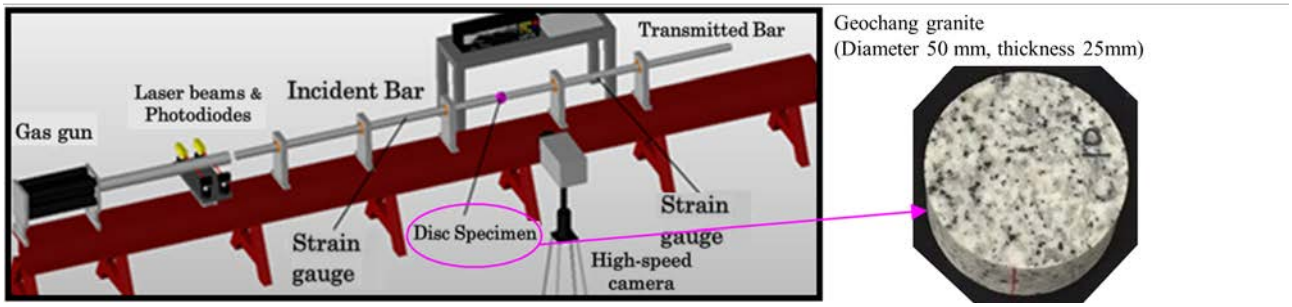

(b) Configuration of SHPB-based dynamic Brazilian test for Geochang granite

Figure 5: Two dynamic rock testing methods modeled in this paper.

σ_{tans} arrives at the free end of the rock specimen, the σ_{tans} is reflected as tensile stress wave and propagates back toward the IB and this causes multiple tensile fractures, also known as spalling fractures, whose planes are approximately perpendicular to the direction of stress wave propagation. On the other hand, in the case of dynamic Brazilian test using the SHPB, the σ_{tans} propagates toward the interface between the target rock disc and one end of another long cylindrical metal bar, i.e. transmitted bar (TB). When the σ_{tans} arrives at the interface, the rock disc is subjected to dynamic compression by both the IB and TB. If the compression forces by the IB and TB are almost equal in magnitude, dynamic indirect tensile stress, which is very similar to the Brazilian test due to static loading, is developed along the centre line of the disc. When the level of the dynamic indirect tensile stress becomes high enough to cause tensile fractures, the rock disc is split into two halves. Although conceptually simple, numerical simulations of these dynamic tests are far from simple and computationally expensive since 3D stress propagation in metal and rock, contact between metal and rock, complex dynamic fracture process in rocks modeled through fine mesh as well as complex contact process between newly created rock fracture surfaces must be considered.

Figure 6 (a) and (b) show the numerical models for the simulations of both the HPB-based spalling test and SHPB-based dynamic Brazilian test, respectively, of Geochang granite obtained in Korea. In these models, the SB is not explicitly modeled and prescribed velocity corresponding to the impact of SB on the one end of the IB is instead applied. This prescribed velocity is determined by the time-history of strain measured by the strain gauge attached on the surface in the middle of IB (see Fig. 6 (a) and (b)). To correctly capture the contact process between metal bars and rock and dynamic fracture process of rock, fine mesh discretization was applied for entire rock part and metal part near the interface between rock and metal bars. Since the authors are still in the process of calibration for these simulations, the following numerical simulations are shown just for demonstration purpose and only qualitative discussion whether our code can capture the typical fracture processes observed in these experiments is made assuming homogeneous rock. In the dynamic simulations, Young's modulus, E_{rock} (= 40.6 GPa), and Poisson's ratio (= 0.2) are computed based on the measured density and elastic wave speed of the granite specimen along the loading direction assuming isotropic elasticity. It is worth mentioning that we have also tested the application of orthotropic elasticity for modelling the anisotropic wave propagation using Eq. (2) for in which elastic parameters are obtained based on "New Self Consistent Scheme (Nara & Kaneko, 2006)". However, the obtained results with/without the consideration of orthotropic elasticity showed negligible difference and thus the results for isotropic elasticity is only discussed. No CE6 was inserted for the metal regions. For CE6s for rock part, T_s = 15 MPa, c = 36.7 MPa, φ = 50° are set considering the quasi-static experimental results, $o_t = s_t$ = 100 μm are just assumed, and $P_f = P_{tan} = P_{overlap} = 50E_{rock}$ were chosen to reduce the decrease of wave speed due to ICZM approach. For the values of contact penalty terms, $P_{n\_con} = P_{tan\_con} = E_{rock}$ are assumed. The value of μ_{fric} for the surfaces of rock-to-rock and rock-to-metal are set to 0.5 and 0.1 respectively.

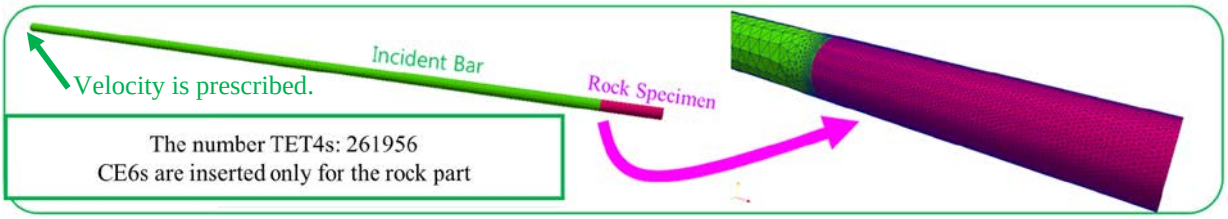

(a) Numerical model for HPB-based dynamic spalling test

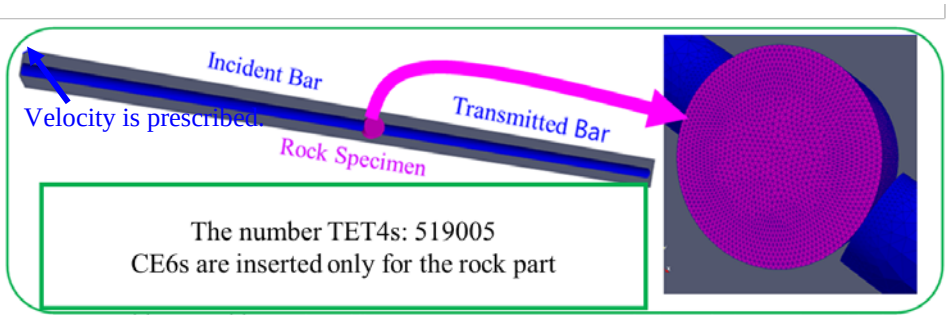

(b) Numerical model for SHPB-based dynamic spalling test

Figure 6: Numerical models for the dynamic rock testing methods in Fig 5.

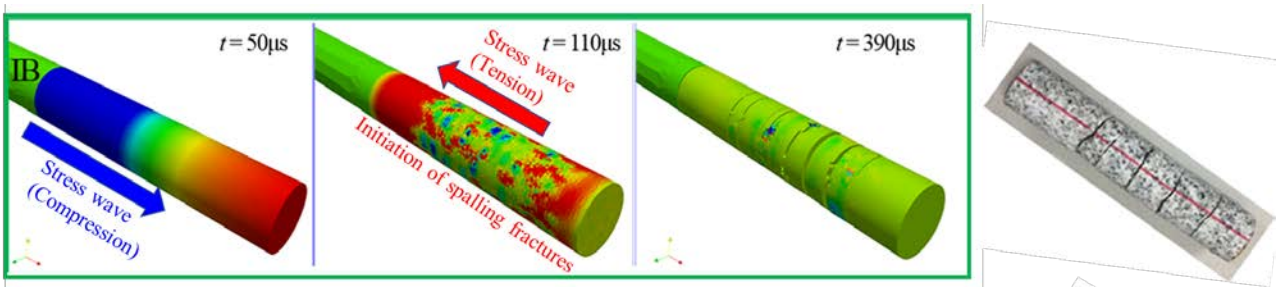

(a) Simulation of HPB-based dynamic spalling test for Geochang granite and fracture pattern experiment

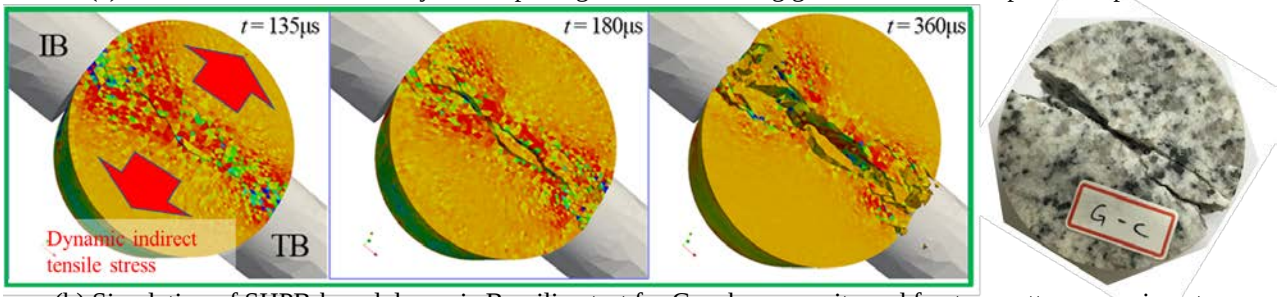

(b) Simulation of SHPB-based dynamic Brazilian test for Geochang granite and fracture pattern experiment

Figure 7: Results of numerical simulations for the dynamic rock testing methods in Fig 5.

Figure 7 shows the examples of dynamic fracture process analyses using 3D YHFDEM IDE parallelized by GPGPU. In these examples, by setting t = 0 when the σ_{inci} in the IB arrives at the interface between the IB and rock, the results of dynamic fracture processes of rock for $t > 0$ are shown for selected time intervals. For the HPB-based spalling test (Fig. 7(a)), as is expected, approximately 1-dimentional compressive stress wave (cold colour), σ_{tans}, propagates toward the free end of the specimen and no fracture occurred during this period. Then, after the compressive wave arrives at the free end and reflected as tensile stress wave (warm colour), the tensile stress wave propagates back toward the IB side during which the multiple spalling fracture planes were developed. By comparing the fracture patterns by the numerical simulation and experiment, it is found that the simulation result can realistically capture the experimentally obtained fracture pattern characterized by multiple spalling fracture planes. For the SHPB-based dynamic Brazilian test (Fig. 7(b)), after the σ_{tans} arrives at the interface between rock disc and TB, it is found that the indirect tensile stress (warm colour) dynamically develops along the centre line of the specimen connecting the IB and TB and this caused the initiation of tensile fractures in the way that the specimen is split into two halves. In addition, because of the high-speed impact between rock and metal, 3-dimentionally complex fragmentation due to shearing was also simulated in which the rock is fragmentated into very small pieces. By comparing the simulated result with the experiment, tensile fracture along the centre line and significant fragmentation near the interfaces with the IB and TB are found to be captured well in the numerical simulation.

4 CONCLUSIONS

This paper explained the algorithm of recently developed 3D Y-HFDEM IDE parallelized by GPGPU with CUDA C/C++. By focusing on modelling lab-scale rock testing methods, the 3D numerical simulations of uniaxial compression and Brazilian test under quasi-static loading, dynamic spalling test using HPB, dynamic Brazilian test using SHPB were demonstrated using the proposed GPGPU-based 3D Y-HFDEM IDE. It was found that the fracture processes for all the simulations are reasonable. In addition, the comparison of simulation time between 3D Y-HFDEM IDE implemented by GPGPU programming and sequential CPU programming showed that GPGPU-based code can run much faster than the sequential code. Through these demonstrations, it was shown that the proposed GPGPU-based 3D Y-HFDEM IDE has a high potential to be applied for the solution of larger scale geotechnical engineering problems in which massive computational effort is required and the CPU-based sequential code is not applicable. However, since the proposed code has been developed just recently, much more verification and validation by comparing with more experimental results must be conducted. In addition, GPGPU implementation to utilize multiple GPGPU cards such as GPGPU cloud/cluster to solve much larger scale problem is another important future task.

ACKNOWLEDGEMENTS

This work was supported by JSPS KAKENHI for Grant-in-Aid for Young Scientists for the first author. The corresponding author would like to thank the supports of AJF (No. 17/20470), AAS (No. RI8) and IRGS (No. L0018929) grants of Australia and National Science Foundation grants (No. 51574060 and No. 51079017) of China, in which the corresponding author is the international collaborator.

References

Ayachit, U. (2015) The paraview guide: a parallel visualization application.

Lisjak, A., Mahabadi, O. K., He, L., Tatone, B. S. A., Kaifosh, P., Haque, S. A. & Grasselli, G. (2018) Acceleration of a 2D/3D finite-discrete element code for geomechanical simulations using General Purpose GPU computing. *Computers and Geotechnics*, 100, 84-96.

Liu, H. Y., Kang, Y. M. & Lin, P. (2015) Hybrid finite–discrete element modeling of geomaterials fracture and fragment muck-piling. *International Journal of Geotechnical Engineering*, 9(2), 115-131.

Lukas, T., Schiava D'Albano, G. G. & Munjiza, A. (2014) Space decomposition based parallelization solutions for the combined finite–discrete element method in 2D. *Journal of Rock Mechanics and Geotechnical Engineering*, 6(6), 607-615.

Mohammadnejad, M., Liu, H., Chan, A., Dehkhoda, S. & Fukuda, D. (2018) An overview on advances in computational fracture mechanics of rock. *Geosystem Engineering*, 1-24.

Munjiza, A., Andrews, K. R. F. & White, J. K. (1998) Combined single and smeared crack model in combined finite-discrete element analysis. *International Journal for Numerical Methods in Engineering*, 44(1), 41-57.

Munjiza, A. A. (2004) *The combined finite-discrete element method*John Wiley & Sons.

Nara, Y. & Kaneko, K. (2006) Sub-critical crack growth in anisotropic rock. *International Journal of Rock Mechanics and Mining Sciences*, 43(3), 437-453.

Rockfield (2005) *Rockfield Software Ltd*, 2005. Available online: http://www.rockfield.co.uk/elfen.htm [Accessed.

Rougier, E., Knight, E. E., Broome, S. T., Sussman, A. J. & Munjiza, A. (2014) Validation of a three-dimensional Finite-Discrete Element Method using experimental results of the Split Hopkinson Pressure Bar test. *International Journal of Rock Mechanics and Mining Sciences*, 70, 101-108.

Xiang, J., Latham, J.-P. & Farsi, A. (2016) Algorithms and Capabilities of Solidity to Simulate Interactions and Packing of Complex Shapes Singapore: Springer Singapore.